Influence of low-Z impurity on the stabilization of m/n = 2/1 tearing/locked modes in EAST

Ming Xu[1], Yunfeng Liang[1,2,3], Lai Wei[4], Yanmin Duan[1], Tonghui Shi[1], Hailin Zhao[1], Liqing Xu[1], Ruijie Zhou[1], Ling Zhang[1], Shuai Gu[1,5,6], Wei Gao[1], Yang Zhang[1], Zhengxiong Wang[4], Qing Zang[1], Haiqing Liu[1], Youwen Sun[1], Liqun Hu[1], Xianzu Gong[1], Guosheng Xu[1], Jiansen Hu[1], Baonian Wan[1], and the EAST Team[1]

[1]*Institute of Plasma Physics, Chinese Academy of Sciences (ASIPP), Hefei 230031, P.R. China*
[2]*Huazhong University of Science and Technology, Wuhan 430074, P.R. China*
3 Forschungszentrum Jülich GmbH, Institut für Energie- und Klimaforschung – Plasmaphysik, Partner of the Trilateral Euregio Cluster (TEC), 52425 Jülich, Germany
[4]*School of Physics, Dalian University of Technology, Dalian, 116024, P.R. China*
[5]*General Atomics, PO Box 85608 San Diego, CA 92186-5608, USA*
[6]*Oak Ridge Associated Universities, Oak Ridge, TN 37830, USA*

(Dated: 15:33 Monday 8th November, 2021)

The impact of the low-Z impurity concentration on the modes stabilization has been investigated in the EAST tokamak. Series of tearing modes (TMs) with multiple helicities are excited by the concentration of low-Z (carbon) impurity, and the dominant mode structure is featured by $m/n = 2/1$ magnetic islands that propagates in electron diamagnetic drift direction (m and n are poloidal and toroidal mode numbers respectively). The $m/n = 2/1$ locked modes (LMs) can be formed by the redistribution of low-Z impurity concentration, which is unlocked spontaneously for the decreasing of impurity concentration, where the width of magnetic islands can be reached $w \approx 5$ cm ($w/a \approx 0.1$, a is minor radius). The increasing of electromagnetic brake torque is the primary reason for the mode locking, and the 'O'-point of $m/n = 2/1$ magnetic islands is locked by the tungsten protector limiter (toroidal position: $-0.4\pi \leq \phi \leq -0.3\pi$) with separation of $\Delta\phi \approx 0$. The 3D asymmetric structure of $m/n = 2/1$ magnetic islands is formed for the interaction with the tungsten protector limiter, and the electromagnetic interaction decreases dramatically for the separation of $\Delta\phi \geq 0.2\pi$. The mechanisms for the mode excitation and locking can be illustrated by the "hysteresis effect" between the low-Z impurity concentration and the width of $m/n = 2/1$ magnetic islands, namely the growth of magnetic islands is modulated by the low-Z impurity concentration, and the rotation velocity is decelerated accordingly. However, the intrinsic mechanism for the unlocking of $m/n = 2/1$ LMs is complicated by considering of the low-Z impurity, and the possible unlocking mechanism is discussed. Therefore, understanding of the relationship between the impurities and magnetic islands is more important for the developing of control techniques, e.g., LMs, NTM and major collapse.

I. INTRODUCTION

The existence of suitable impurity ions is important in fusion devices for a variety of reasons [1–3], which have been assessed of the impurity radiation in the core and divertor plasmas for ITER and DEMO [4]. However, series of tearing modes (TMs) instabilities can be triggered by the concentration of impurities [5–10], and the structure of magnetic islands are formed accordingly as Refs [11]. The interaction between the impurity density and TMs instability is more dangerous for the plasma confinement, e.g., the formation of locked modes (LMs) [12] or the triggering of major disruption [13, 14]. The LMs can be unlocked by the resonant magnetic perturbations (RMP), which have been applied extensively [15–18]. The rotation of magnetic islands can be decelerated by the electromagnetic interaction with wall of finite resistivity [19], which can be driven by the viscous coupling of the modes with the bulk plasma [18, 20, 21]. Interestingly, the multiple helicities of TMs are excited by the influx of low-Z impurity in EAST, and the $m/n = 2/1$ LMs can be formed and unlocked spontaneously by the redistribution of low-Z impurity concentration (m and n are poloidal and toroidal mode numbers respectively). Furthermore, the intrinsic mechanism of mode stabilization of magnetic islands by considering of low-Z impurity is more important in validating the physical model of mode locking [18], which are motivated the current work.

The rotation velocity of magnetic islands can be braked (accelerated) respectively for the increasing (decreasing) of low-Z impurity concentration. The "hysteresis effect" of the width (w) of $m/n = 2/1$ magnetic islands versus low-Z impurity concentration is formed accordingly that has been observed in the EAST tokamak, namely the electromagnetic brake torque can be modulated by the low-Z impurity concentration. In the rest of the paper, the schematic of EAST device and partial diagnostics are given in section II. The basic discharge condition, modes excitation, mode locking/unlocking of $m/n = 2/1$ magnetic islands are summarized in section III, and the "hysteresis effect" between w and low-Z impurity concentration is demonstrated in section IV, and the conclusion and discussion are presented in section V. The $m/n = 2/1$ and $m/n = 4/1$ magnetic islands at different rational surfaces are coupled together and rotated by the same frequency as documented in the Appendix, and the structure of 3D asymmetry is formed accordingly.

II. EXPERIMENTAL SETUP

Experimental Advanced Superconducting Tokamak (EAST: major radius $R_0 \leq 1.9$ m and minor radius $a \approx 0.45$ m) with shaped poloidal cross-section as shown in figure 1. Several diagnostics are equipped on different horizontal ports that are marked by A, B, $\cdots$, P respectively, and the $\phi = 0$ is defined as the center position between ports P

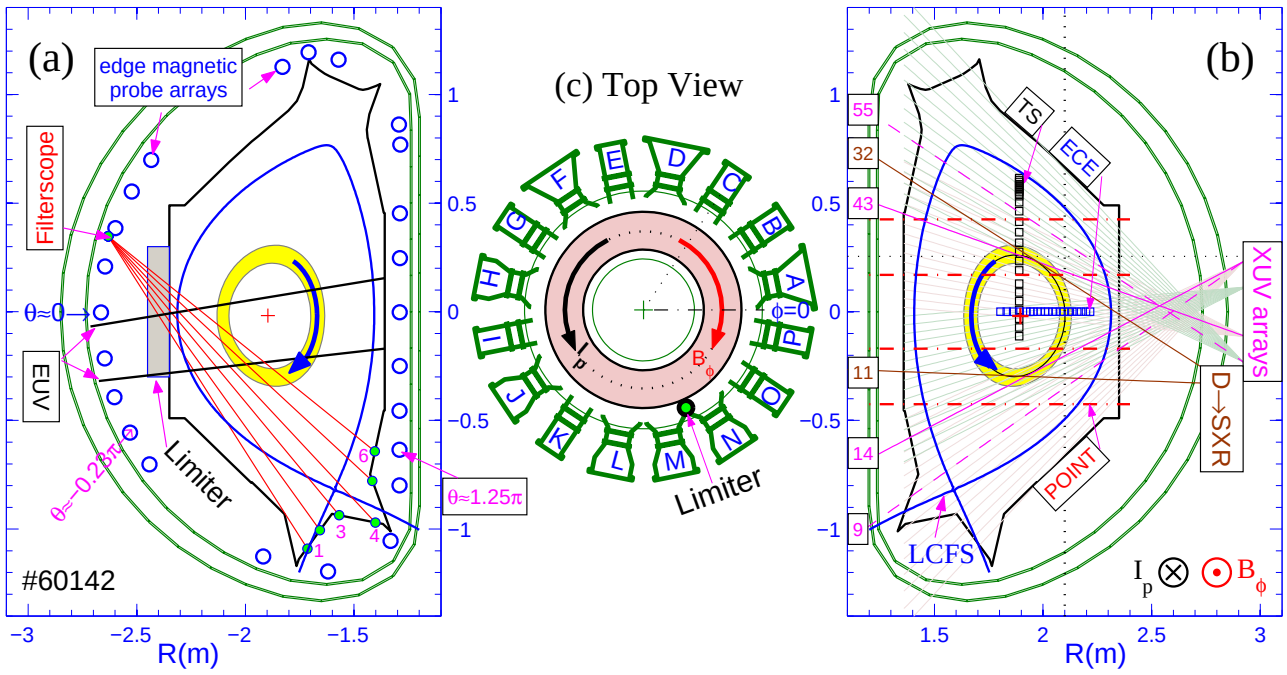

FIG. 1: Schematic diagrams of EAST top view (c) and side views in (a) and (b), where the poloidal position (yellow shaded region) and rotation direction (blue bold arrow) for the m/n = 2/1 magnetic islands are marked schematically.

and A along toroidal direction. The carbon impurity can be detected by the Filterscope [22] and flat-field extreme ultraviolet (EUV) [23] spectrometer directly, which can also be speculated from absolute extreme ultraviolet (XUV) [24] arrays indirectly. The Filterscope and EUV spectrometer are mounted in the horizontal ports G and D respectively, and the line emissions of CIII (edge) and CVI (core) can be monitored accordingly. The detector of XUV array is sensitive to photons in the wavelength of 0.2 nm - 1.2×10^3 nm, and the CIII (Filterscope: edge) and CVI (EUV: core) signals with wavelengths of 465 nm and 3.37 nm can be monitored concurrently. Furthermore, the electron density n_e and electron temperature T_e are increased and radiated accordingly by the influx of low-Z impurity. The n_e is measured by Polarimeter Intferometer (POINT) [25] array, which distributes uniformly along the vertical direction of port O. The T_e are measured by the second harmonics mode of heterodyne radiometer of electron cyclotron emission (ECE) [26, 27] and Thomson scattering (TS) [28] diagnostics respectively, and the ECE signals can be calibrated by the measurement of TS array. The two arrays (ECE and TS) are located in ports P and L respectively as shown in figure 1(c), which are separated by $\Delta\theta \approx \pi/2$ (poloidal) and $\Delta\phi \approx \pi/2$ (toroidal).

Two sets of edge magnetic pickup arrays with the similar arrangements are situated at ports C and K, and the toroidal positions are $\phi_C \approx 0.31\pi$ and $\phi_K \approx -0.69\pi$ accordingly. Two soft X-ray (SXR) arrays are equipped on the horizontal port P, and the detectors located on the bottom section is labelled by the alphabet of D. Magnetic surfaces with normalization radius (r/a) are reconstructed from the edge magnetic measurements. The sight-lines of SXR and XUV detectors are tangent to a series of poloidal magnetic surfaces, and the points of tangency are defined as $\rho_{sxr}(r/a)$ and $\rho_{xuv}(r/a)$. The field of view of SXR and X-UV detectors are fully different, and the relative positions of $\rho_{sxr}(r/a) \approx \pm 0.5$ and $\rho_{xuv}(r/a) \approx \pm 0.5$ are demonstrated in figure 1(b) for the SXR channels (11 and 32) and XUV channels (14 and 43) respectively, where $\rho_{sxr,xuv}(r/a) < 0$ means the point of tangency locates in the bottom section. The tungsten protector limiter locates between ports M and N with $-0.4\pi \leq \phi_{Lim} \leq -0.3\pi$, and the distance between the limiter and last closed flux surface (LCFS) is ~3.7 cm. The EAST has equipped with a molybdenum first wall, a SiC-coated graphite lower divertor and a ITER-like W/Cu upper divertor [29]. The low-Z (carbon) impurity is generated easily under the magnetic configuration of lower single-null (LSN) divertor due to the plasmas wall interactions, where the high-Z (tungsten) impurity can be produced for the configuration of upper single-null (USN).

III. EXPERIMENTAL RESULTS

The experiments are performed in L-mode plasmas with low beta ($\beta_p \leq 1$), and the magnetic configuration of #61042 with LSN is demonstrated in figure 1, where the opening direction of 'X'-point of LCFS deviates inward. The ion $\mathbf{B} \times \nabla\mathbf{B}$ drift direction is downward. The core electron temperature and line-integrated electron density are $T_{e0} > 2$ keV and $\langle n_{e0} \rangle > 2 \times 10^{19} m^{-3}$ respectively, and the B_ϕ·R ≈ -4.16 T·m (the sign of '-' means the directions of toroidal magnetic field B_ϕ and plasma current I_p = 0.4 MA are reversed, R is major radius), $q_{95} \approx 7$ (edge safe factor at 95% poloidal magnetic flux surface), magnetic axis $(R_m, Z_m) \approx$ (1.89,-0.02) m, elongation $\kappa \approx 1.75$, internal inductance $l_i \leq$

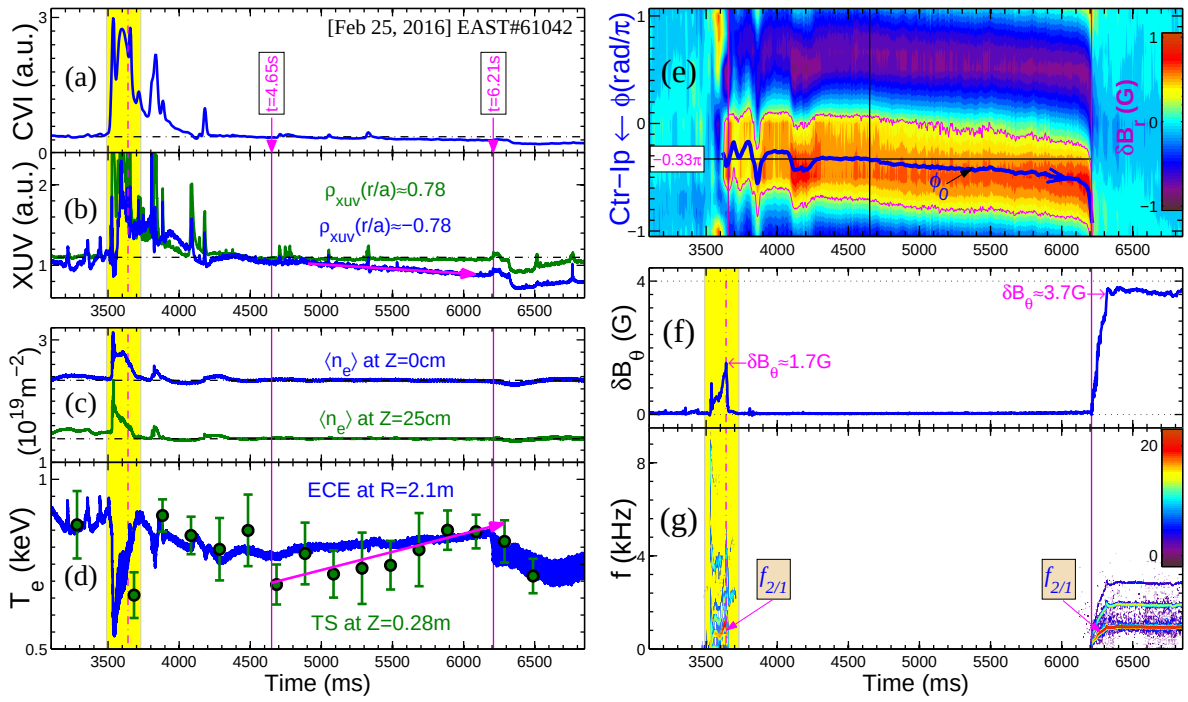

FIG. 2: Basic discharge condition for shot #61042. (a) core integrated intensity of CVI signal measured by the EUV spectrometer, (b) two channels (#9 and #55) of XUV signals with $\rho_{xuv} \approx \pm 0.78$ are marked in figure 1(b), (c) line-integrated electron densities $\langle n_e \rangle$ measured by POINT array, (d) the T_e at q = 2 surface are measured by ECE and TS arrays respectively, (e) δB_r and ϕ_0 for locked $n = 1$ magnetic island are measured by the saddle loops as Ref [30], (f) poloidal magnetic component δB_θ for $m/n = 2/1$ TMs intensity, and the spectrogram of edge magnetic signal is given in (g).

1.4, and the upper and lower triangularity are $\delta_u \approx 0.49$ and $\delta_l \approx 0.6$ respectively. The loop voltage is $U_t \approx 0.1$ V, namely the dominating portion of plasma current is driven by lower hybrid wave (LHW) with power of $P_{LH} \approx 1.6$ MW.

The carbon (low-Z) impurity is generated from the lower divertor, which can be monitored synchronically by the measurements of Filterscope and XUV arrays respectively. The line emission of CIII signals erupts abruptly from the lower inner divertor, which are observed successively by the two chords #3 and #4 of Filterscope signals. Such process is captured by the XUV array, and the two spots are observed in the region of $\rho_{xuv}(r/a) \leq$ -0.8 for t ≤ 3.53 s as shown in figure 3(a). The counts of the core integrated intensity of CVI signal increases by tenfold as shown in figure 2, and the intensities of the XUV, electron density and temperature signals are altered accordingly for the influx of low-Z impurity, e.g., the core line-integrated electron density increases by $\Delta n_e/n_e \geq 17\%$, and the electron temperature at q = 2 surface decreases by $\Delta T_e/T_e \geq 50\%$.

The $m/n = 2/1$ TMs with the rotation frequency $f_{2/1}$ are excited by the concentration of low-Z impurity, and the oscillation amplitude of $m/n = 2/1$ magnetic islands achieves by the maximum for the moment of t = 3.64 s. The structure of $m/n = 2/1$ LMs is formed (t ≥ 3.66 s) and unlocked (t ≥ 6.21 s) spontaneously as demonstrated in figure 2(e)-(g). It needs to be stressed that the mode features (excitation, locking and unlocking) of the $m/n = 2/1$ magnetic islands have strong relationship with the carbon concentration, which will be discussed as follows.

A. Modes excitation

Series of TMs with different frequencies ($f_{4/1}$, $f_{3/1}$, $f_{2/1}$ and $f_{3/2}$) and multiple helicities ($m/n = 4/1$, $m/n = 3/1$, $m/n = 2/1$, and $m/n = 3/2$) are excited successively, as shown in figure 3. The relative positions of those modes are located at $\rho(r/a) \approx 0.8$ (q = 4, R ≈ 2.23 m), $\rho(r/a) \approx 0.65$ (q = 3, R ≈ 2.17 m), $\rho(r/a) \approx 0.5$ (q = 2, R ≈ 2.1 m or R ≈ 1.67 m in HFS), and $\rho(r/a) \approx 0.39$ (q = 1.5, R ≈ 2.06 m) respectively, and those modes are propagated in electron diamagnetic drift direction that is marked by the blue bold arrow as shown in figure 1. The excitation of those TMs instabilities have strong relationship with the carbon concentration, and one example is selected as demonstrated in figure 4.

The $m/n = 4/1$ TMs with frequency $f_{4/1} \approx 8$ kHz is excited temporally ($\Delta t \leq 2$ ms) for the moment of t ≈ 3.531 s. The special region with $\delta I_{xuv}/\bar{I}_{xuv} \geq 35\%$ is observed in the bottom section (-0.73 ≤ $\rho_{xuv}(r/a)$ ≤ -0.86) that encompassed by the blue enclosed curve, which is fully covered the q = 4 surface. Interestingly, the $m/n = 4/1$ TMs is excited synchronically for the concentration of low-Z impurity. The structure of magnetic islands propagates in counter-current direction, and the toroidal mode number $n = 1$ can be estimated by the two channels that separated by π toroidally as shown in figure 4(b). The phase angle α_{12} of magnetic islands increases in the counter-clockwise direction along poloidal as shown in figure 4(c), and the phase displacement is $\Delta\alpha_{12} = 8\pi$ for one poloidal circle, namely the poloidal mode number is $m \equiv \Delta\alpha_{12}/2\pi = 4$. Furthermore, the down/up asymmetric of $m/n = 4/1$ magnetic is-

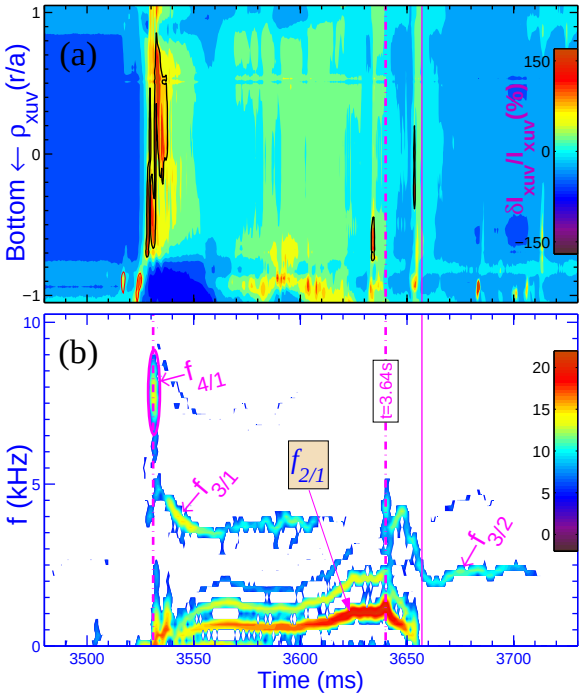

FIG. 3: The concentration of low-Z impurity and the excitation of different helicities of TMs instabilities. Definition: the relative fluctuation is $\delta I_{xuv} = I_{xuv} - \bar{I}_{xuv}$, and the $\bar{I}_{xuv}$ is the averaged intensity for the selected time interval.

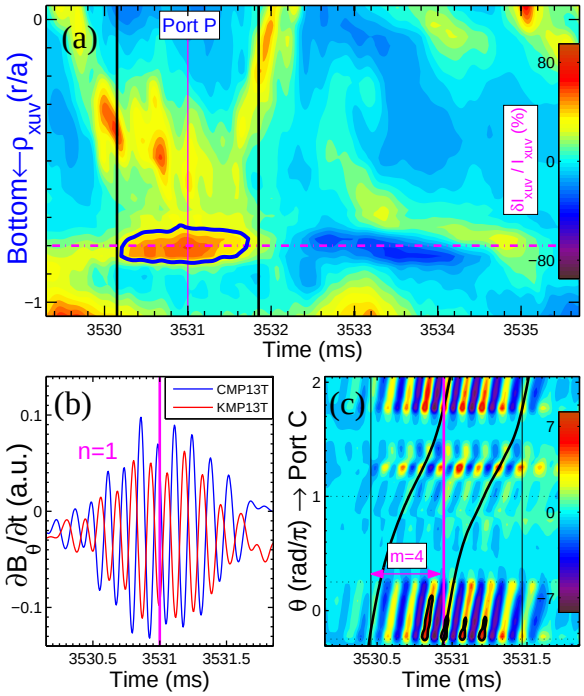

FIG. 4: The excitation of m/n = 4/1 TMs and the concentrating of low-Z impurity are observed synchronically, and the q = 4 surface with $\delta I_{xuv}/\bar{I}_{xuv} \geq 35\%$ is encompassed by the blue curve as shown in (a).

lands is observed for the current condition. The oscillation of TMs ($f_{4/1}$) can only be observed by the three chords of XUV array that is fully covered by the blue enclosed curve as shown in figure 4(a), and the similar oscillation is also be observed by the POINT array for the chord with Z = -43 cm, which are confirmed by the edge magnetic signals as shown in figure 4(c), i.e., the down/up asymmetry.

The excitation of m/n = 2/1 TMs by the concentrated of low-Z impurity is demonstrated in figure 5. The time evolution of carbon concentration can be speculated by the measurements of XUV and ECE arrays. The line emission of different ionization states of low-Z (carbon) impurity can be monitored entirely by the measurement of XUV array, and the intensities I_{xuv} increase by the twofold for the moment of t ≈ 3.54 s. The T_e is radiated accordingly by the concentrating of low-Z impurity [31], and the intensities of ECE signals decreases dramatically for the same moment of t ≈ 3.54 s. Interestingly, the maximum alteration of $\Delta T_e/T_e$ is reached at 50% for the shaded region of q = 2 surface with normalized minor radius $\rho(r/a) \approx 0.5$ (R ≈ 2.1 m). Therefore, the m/n = 2/1 TMs should be excited by the concentration of low-Z impurity.

The up/down asymmetry of low-Z impurity concentration is observed by the measurement of XUV signals. The intensities of I_{xuv} for the top section ($0.5 \leq \rho_{xuv}(r/a) \leq 0.8$) is nearly twice larger than the bottom section for the moment of t ≈ 3.54 s, which is in accordance with the measurements in C-Mod [32] that the impurity density is larger on the side opposite to the ion $\mathbf{B} \times \nabla\mathbf{B}$ drift direction. The up/down symmetry is restored gradually for the decreasing of carbon concentration. The I_{xuv}-profiles for the two moments of t

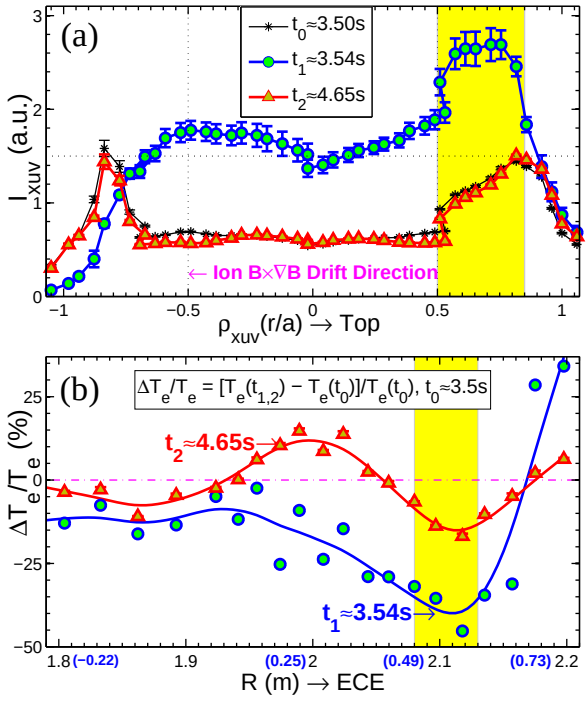

FIG. 5: The low-Z impurity concentration is speculated by the combination of XUV and ECE arrays. Note: the $\Delta T_e/T_e = [T_e(t_{1,2}) - T_e(t_0)]/T_e(t_0)$ is defined, and the normalized minor radius $\rho(r/a)$ for the four radial positions are marked by the blue font in (b).

= 3.5 s and t = 4.65 s are nearly the same, while the relative alterations electron temperature are $\Delta T_e/T_e \approx 15\%$ and $\Delta T_e/T_e \leq$ -15% respectively for the two regions of R ≈ 2

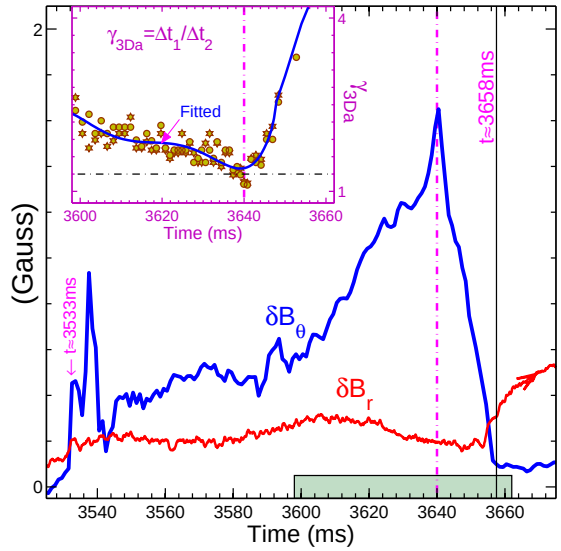

FIG. 6: The modes locking of $m/n = 2/1$ magnetic islands. Definition: $\gamma_{3Da} = \Delta t_1/\Delta t_2$, Δt_1 and Δt_2 are given in Fig. 14(a).

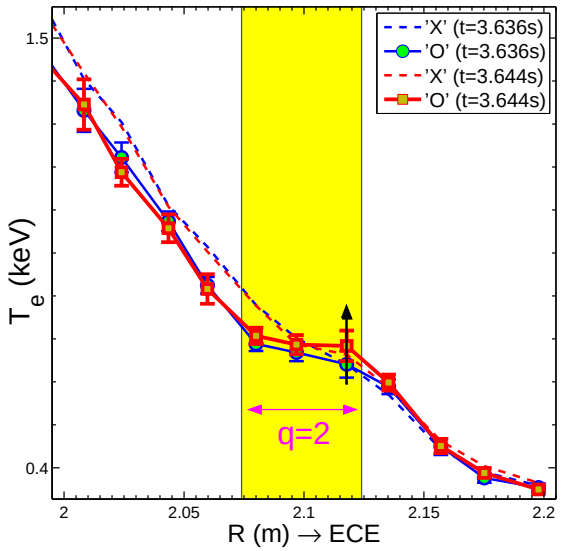

FIG. 7: The structures of 'O' and 'X' points of $m/n = 2/1$ magnetic islands for two different moments.

m and R ≈ 2.1 m. Therefore, the T_e-profile is modified by the alteration of impurity concentration, and the gradient of $dT_e/dR|_{q=2}$ in the region of 2 m ≤ R ≤ 2.1 m increases accordingly for the comparison of the two moments of t = 3.5 s and t = 4.65 s.

B. Mode locking

The structure of $m/n = 2/1$ magnetic islands is locked for the moment of t ≈ 3.66 s as shown in figure 6. The δB_θ increases dramatically for t ≥ 3.53 s, and the dominant structure ($m/n = 2/1$ TMs) is observed for the moment of t ≈ 3.533 s. The δB_θ increases gradually for t ≥ 3.6 s, which achieves the maximum for the moment of t ≈ 3.64 s with $\delta B_\theta \approx 1.7$ Gauss ($\delta B_\theta/B_{\phi 0} \sim 10^{-4}$, toroidal magnetic field $B_{\phi 0} \approx 2$ T). Interestingly, the inflection point can also be observed from the 3D asymmetric index γ_{3Da} for the same moment of t ≈ 3.64 s as shown in the small rectangular box of figure 6, which is defined in the Appendix. The rotation frequency $f_{2/1}$ and oscillation amplitude δB_θ decrease simultaneously for the time interval of 3.64 ≤ t ≤ 3.66 s, i.e., the rotation frequency of $m/n = 2/1$ magnetic islands is locked gradually. The radial magnetic component δB_r and spatial phase angle ϕ_0 for the LMs are measured by the saddle loops as shown in figure 2(e), which can be expressed as Ref [30]: $\delta B_r = B_{r0} \cdot \cos(n\phi - \phi_0)$, where eight magnetic loops are equipped in LFS of equatorial plane along toroidal direction ϕ. The $n = 1$ magnetic island is locked by the tungsten protector limiter ($-0.4\pi \le \phi_{Lim} \le -0.3\pi$) for t ≥ 3.66 s, and the 3D intrinsic error fields are formed accordingly. Furthermore, the rotation frequency of $m/n = 3/2$ magnetic islands decreases synchronously ($f_{3/2} = 4 \rightarrow 2.3$ kHz) during the mode locking of $m/n = 2/1$ magnetic islands, namely the brake torque increase similarly for the two q = 1.5, 2 rational surfaces (R = 2.06 ,2.1 m).

The electromagnetic brake torque is the primary reason for the mode locking of $m/n = 2/1$ magnetic islands. The width of the 'O'-point of $m/n = 2/1$ magnetic islands can be estimated by the locally flattened T_e-profile, which is marked by the shaded region of figure 7, where the 'O' and 'X' points of magnetic islands are represented by solid and dash lines respectively. The width (w) of $m/n = 2/1$ magnetic islands increases obviously for the time interval of t = 3.636 → 3.644 s, which is marked by the black arrow. Therefore, the electromagnetic brake torque ($F_{RW} \propto w^4$) is the primary reason for the mode locking, and the maximum width of magnetic islands can be reached at $w \approx 5$ cm ($w/a \ge 0.1$).

C. Mode unlocking spontaneously

The $m/n = 2/1$ LMs is unlocked spontaneously as demonstrated in figure 8. The central position (ϕ_0) of locked magnetic islands deviates from the initial position ($\phi_0 \approx -0.33\pi$) gradually, which propagates in counter current direction as marked by the blue arrow. The alteration of ϕ_0 for the two stages (t = 4.65 → 6.17 s and t = 6.17 → 6.207 s) are nearly the same as $\Delta\phi_0 \approx \pi/4$, while the time interval (Δt) are $\Delta t \approx 1.52$ s and $\Delta t \approx 0.037$ s respectively, i.e., the rotation velocity ($v = d\phi_0/dt$) of 'O'-point of magnetic islands are $v \approx 0.2\pi/s$ and $v \approx 6.8\pi/s$. The slowly rotating of magnetic islands can be captured synchronically by the measurement of ECE array. The 'X'-point of magnetic islands is fully captured for the moment of t = 6.17 s, and the 'O'-point shifts to the toroidal position of $\phi_0 \approx -0.58\pi$ that is separated by $\Delta\phi \approx \pi/2$ from the ECE array ($\phi_p \approx -0.08\pi$). The ECE signal at q = 2 surface increases slowly and decreases swiftly during the time interval t = 4.65 → 6.207 s, and one quarter poloidal period of TMs oscillation is observed, which is in accordance with the alteration of $\Delta\phi_0 \approx \pi/2$. Furthermore, the rotation of 'X'-point of magnetic islands can also be captured by the SXR array during the time interval t = 6.17 → 6.21 s. In the end, the rotation frequency $f_{2/1}$

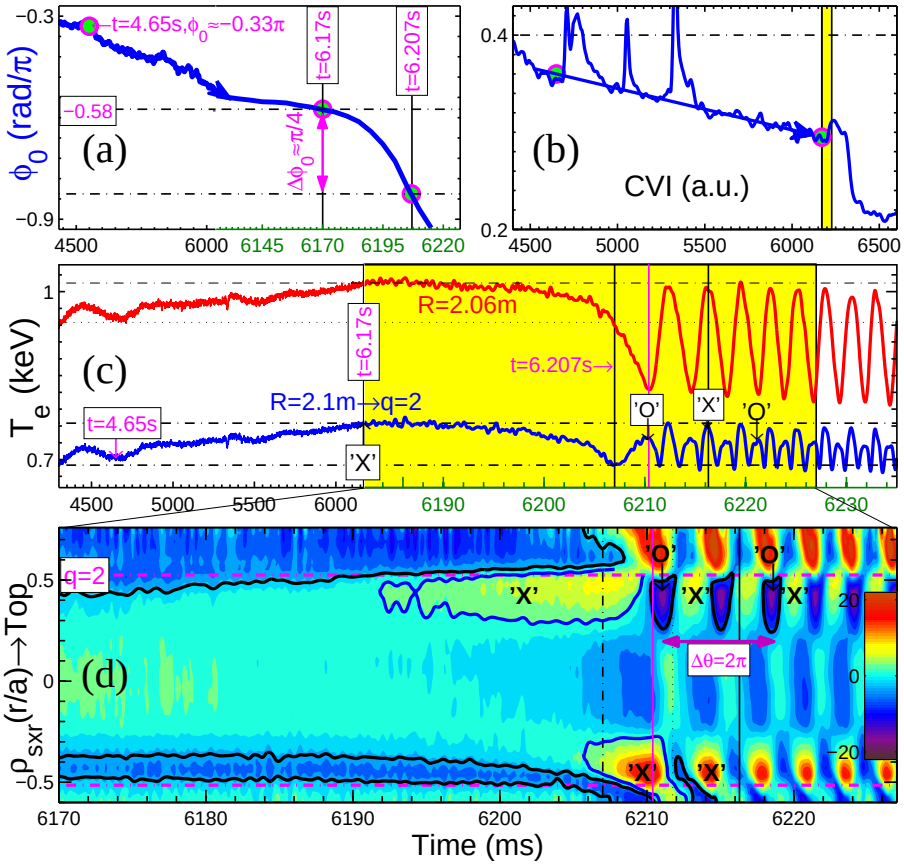

FIG. 8: The m/n = 2/1 LMs are unlocked spontaneously. (a) ϕ_0 of the n = 1 LMs, (b) core integrated intensity of CVI signal, (c) electron temperatures for two radial positions, and the relative alteration of $\delta I_{sxr}/I_{sxr}$ for the shaded region of (c) is amplified and given in (d). Note: the linearity of the x-axis are broken in (a) and (c).

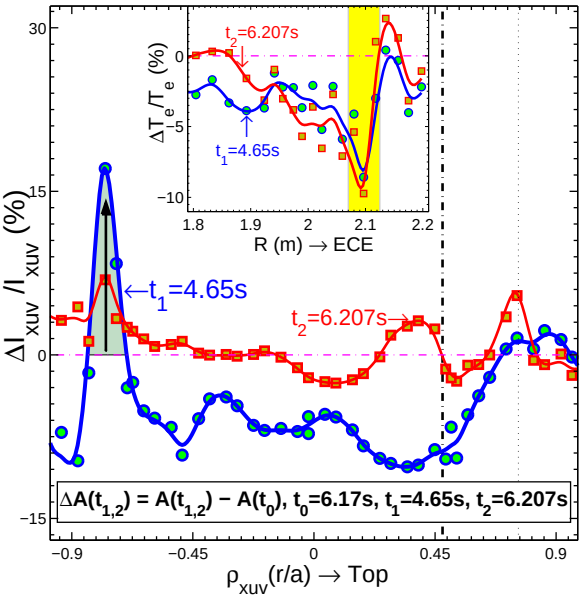

FIG. 9: The relative alterations of $\Delta I_{xuv}/I_{xuv}$ and $\Delta T_e/T_e$ for the XUV and ECE arrays respectively.

restores gradually for t ≥ 6.21 s, namely the transition from LMs to TMs is taken place accordingly.

The carbon concentration decreases synchronically during the mode unlocking. The carbon concentration decreases by $\Delta I_{CVI}/I_{CVI} \approx 17\%$ (t = 4.65 → 6.17 s) as shown in figure 8(b), which is captured by the XUV array for the bottom section as shown in figure 2(b), where the alteration is down/up asymmetry. Fortunately, the maximum alteration of $\Delta I_{xuv}/I_{xuv} \approx 17\%$ is achieved in the region with -0.84 ≤ $\rho_{xuv}(r/a)$ ≤ -0.7 as shown in figure 9, namely the carbon impurity concentration at q = 4 surface is expelled outward. Therefore, the unlocking of m/n = 2/1 LMs is accompanied by the decreasing of low-Z impurity concentration at q = 4 surface.

Some other features are summarized for the structures of magnetic islands. Firstly, the alteration of electron temperature during the mode unlocking is caused by the rotation of 'X'-point of m/n = 2/1 magnetic islands. The $\Delta T_e/T_e \approx$ -10% is achieved for the region of q = 2 surface, which are similar for the two moments t_1 and t_2 as demonstrated in the small rectangle box of figure 9, namely the alteration of T_e during the time interval of t = 4.65 → 6.207 s is caused by the rotation of 'X'-point of m/n = 2/1 magnetic islands. The relative alterations of $\Delta I_{xuv}/I_{xuv}$ are quite different for the two moments t_1 and t_2 owing to the decreases of low-Z impurity concentration. Secondly, the magnetic islands at q = 2, 4 surfaces are coupled together and rotated by the same velocity, which will be discussed in the Appendix. Thirdly, the asymmetric structure is observed for the m/n = 2/1 magnetic islands. The 'X'-points of m/n = 2/1 magnetic islands

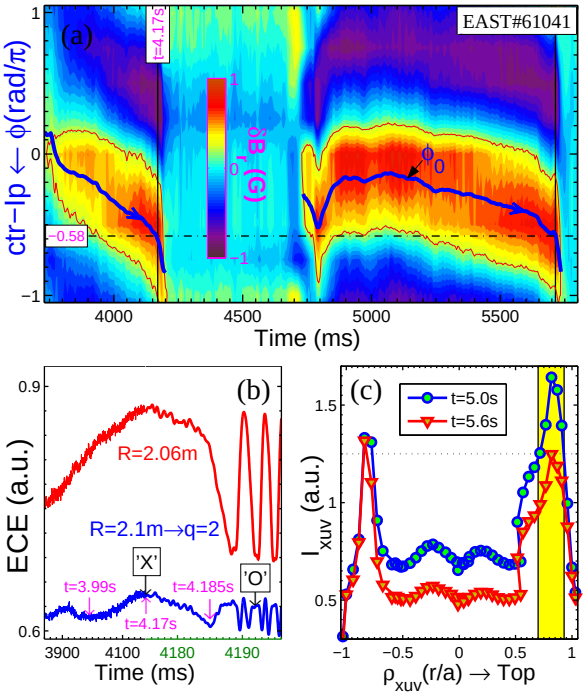

FIG. 10: The structure of m/n = 2/1 magnetic islands is locked and unlocked spontaneously for #61041. (a) δB_r and ϕ_0 for n = 1 LMs, (b) the raw ECE signals for the first stage, and the relative intensities of XUV array for the second stage are given in (c). Note: the linearity is broken for the x-axis in (b).

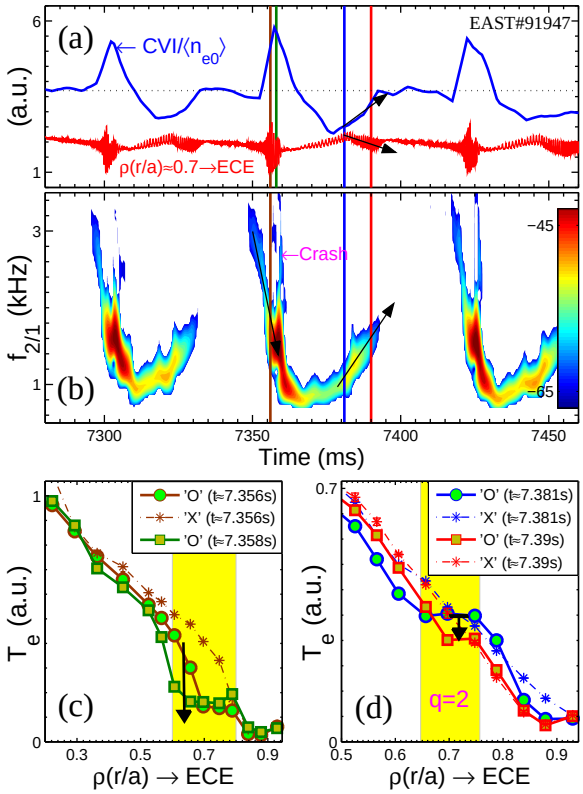

FIG. 11: Relationship between the width of magnetic islands versus the low-Z impurity concentration. (a) are the ECE and core line-integrated CVI signals, (b) spectrogram of edge magnetic signal, and the relative T_e-profiles measured by ECE array for different moments are given in (c) and (d) respectively.

are captured by the SXR array successively on top (t ≈ 6.19 s) and bottom (t ≈ 6.206 s) sections respectively, as shown in figure 8(d). The time delay should be caused by the toroidal asymmetry, as discussed in the Appendix.

The structure of m/n = 2/1 magnetic islands can be locked and unlocked repeatedly, as demonstrated in figure 10. The n = 1 magnetic island is locked by the protector limiter with $-0.4\pi \le \phi \le -0.3\pi$, and two different stages are observed for the time intervals of t = 3.75 → 4.2 s and t = 4.75 → 5.72 s respectively. Interestingly, the inflection point of $\phi_0 \approx -0.58\pi$ is also observed for the two stages, namely the brake torque decreases dramatically when the distance between the 'O'-point of magnetic islands and tungsten protector limiter is separated by $\Delta\phi \ge 0.2\pi$ toroidally. The position of the 'X'-point of magnetic islands can be fully captured by the ECE array for the moment of t = 4.17 s, is demonstrated in the firstly stage. The rotation velocity are $v \le 1.4\pi/s$ and $v \ge 16\pi$ respectively before and after the inflection point of $\phi_0 \approx -0.58\pi$. The low-Z impurity concentration decreases with mode unlocking of m/n = 2/1 magnetic islands, is demonstrated in the second stage. The intensities of XUV signals decrease dramatically, and the up/down symmetry is restored accordingly.

IV. HYSTERESIS EFFECT

The features (width and rotation frequency) of m/n = 2/1 magnetic islands are modulated by the low-Z impurity concentration. One example of shot #91947 is selected as shown in figure 11, and the q = 2 surface with $\rho(r/a) \approx 0.7$ shifts outward for the alteration of q-profile (USN: $q_{95} \approx 6.4$ and $l_i \approx 1.5$). The concentration of low-Z impurity and the structure of m/n = 2/1 magnetic islands are speculated by the measurement of ECE array, and two fully different stages are observed. **Firstly**, the rotation frequency $f_{2/1}$ sweeps downward for the increasing of w in the first stage (7.35 s ≤ t ≤ 7.36 s). The T_e is radiated by the concentrating of low-Z impurity, and the width of m/n = 2/1 magnetic islands increases accordingly, which are marked by the black arrow as shown in figure 11(c). The minor collapse is triggered for the moment of t ≈ 7.36 s, and the width of the flattened region of T_e-profile can be reached at $w/a \ge 0.2$. **Secondly**, the rotation frequency $f_{2/1}$ restores upward for the decreasing of w in the second stage (7.38 s ≤ t ≤ 7.4 s). The T_e for external region with $\rho(r/a) \ge 0.65$ decreases for the concentration of low-Z impurity, while the w of m/n = 2/1 magnetic islands decrease accordingly that is marked by the black arrow as shown in figure 11(d). The width of m/n = 2/1 magnetic islands for the two stages are increased and decreased respectively, which can be illustrated by the hysteresis loops as shown in figure 12.

Hysteresis effect between the width of m/n = 2/1 magnetic islands versus carbon concentration is established. The width of magnetic islands can also be qualitatively described by the formula of $w \propto \delta B_\theta^{1/2}$, and the two stages can be illustrated for one period (t = 7.345-7.395 s) as shown in figure

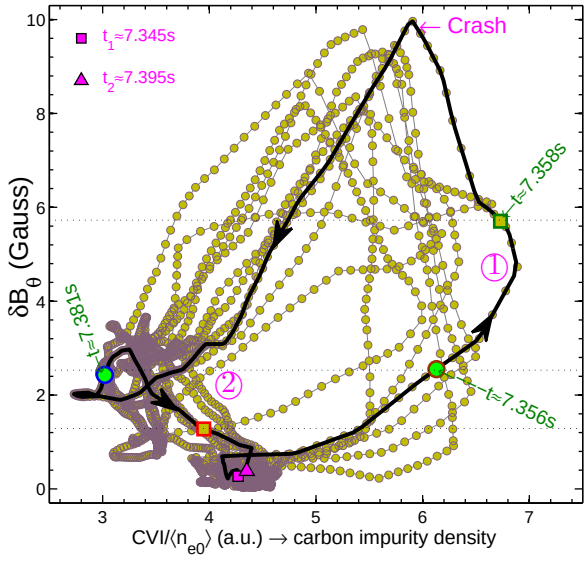

FIG. 12: Hysteresis effect between the width (magnetic islands) versus impurity concentration (carbon). Note: the four different moments in figure 11(c) and (d) are marked schematically.

12. The w increases swiftly with carbon impurity concentration in the first stage, and the $\delta B_\theta \approx 10$ Gauss for the minor collapse (t ≈ 7.36 s). The w decreases for the outward transport of carbon impurity concentration. The w decreases further with the slightly increasing of carbon concentration in the second stage. The hysteresis effect of w versus carbon concentration is clearly observed, and the hysteresis loops are formed accordingly. Therefore, the w of m/n = 2/1 magnetic islands is modulated by the alteration of low-Z impurity concentration, and the "hysteresis effect" should be caused by the slowly altering of current diffusion time.

V. CONCLUSION AND DISCUSSION

The carbon impurity concentration is measured by EUV spectrometer, and the distribution can be monitored indirectly by the measurements of ECE and XUV arrays. The features (mode numbers, spatial structures and positions) of tearing/locked modes are achieved by the measurements of edge magnetic pickup, SXR, ECE, POINT arrays.

Three important results on the relationship between the low-Z impurity concentration and the tearing/locked modes are summarized as follows. (1) Series of TMs with multiple helicities (m/n = 4/1, m/n = 3/1, m/n = 2/1, and m/n = 3/2) are excited successively by the influx of low-Z (carbon) impurity concentration, and the excitation of TMs instabilities and the concentration of low-Z impurity are observed synchronically. (2) The m/n = 2/1 LMs can be formed by the redistribution of impurity concentration, and the 'O'-point of magnetic islands is locked by the tungsten protector limiter with toroidal separation of $\Delta\phi \approx 0$, where the electromagnetic interaction decreases dramatically when the separation of $\Delta\phi \geq 0.2\pi$ is satisfied. The unlocking of m/n = 2/1 LMs and the decreasing of low-Z impurity concentration at q = 4 surface are taken place concurrently. (3) The "hysteresis effect" of carbon impurity concentration on the growth of the width of m/n = 2/1 magnetic islands is observed, and the hysteresis loops are formed accordingly.

Two related results of modes coupling and 3D asymmetry are achieved. (1) The magnetic islands at q = 2, 4 surfaces are coupled together and rotated by the same frequency. The total component δB_θ increases dramatically after the modes coupling of m/n = 2/1 and m/n = 4/1 magnetic islands, and the application of the formula $w_{2/1} \propto \delta B_\theta^{1/2}$ should be cautious for the estimating of width of magnetic islands. (2) The 3D asymmetric structure of m/n = 2/1 magnetic islands is formed by the interaction of tungsten protector limiter. The rotation velocity of m/n = 2/1 magnetic islands is accelerated and decelerated respectively when the 'O'-point is close to and far away from the protector limiter respectively, and the poloidal symmetric structure of magnetic islands is twisted accordingly.

The plasma resistivity can be altered by the low-Z impurity concentration, which should be reason of modes excitation. The effective charge number Z_{eff} increases for the concentration of low-Z impurity, e.g., the Z_{eff} increases by 3.5 times for the moment of t ≈ 3.54 s of #61042, and the T_e drops by one half. The resistivity η increases by tenfold ($\eta \propto Z_{eff} T_e^{-3/2}$), and the width of magnetic islands increases with the low-Z impurity concentration ($dw/dt \propto \eta$). The accumulation of impurity concentration inside the magnetic island has a destabilizing effect on the growth of TMs, which has been performed and verified by the toroidal resistive MHD code CLT [10]. As a result, the TMs can be excited by the concentration of low-Z impurity, and the LMs is formed accordingly for the further increases of width of magnetic islands.

The total torque can be expressed as: $\Sigma F = F_{VS} - F_{RW}$, and the two items F_{VS} and F_{RW} are the viscous accelerating and electromagnetic brake torques respectively. The m/n = 2/1 LMs are unlocked spontaneously during the decreasing of low-Z impurity concentration at q = 4 surface, which means the torque balance is broken by the redistribution of low-Z impurity concentration. Firstly, the effective charge number Z_{eff} at the vicinity of q = 4 surface should be decreased for the outward transport of low-Z impurity concentration, and the intrinsic angular momentum ω_0 increases for the conservation of torque/momentum. Secondly, the electromagnetic coupling of m/n = 4/1 and m/n = 2/1 magnetic islands is beneficial for the spontaneously unlocking of m/n = 2/1 LMs. Therefore, the residual/additional torque ($\Sigma F > 0$) on the m/n = 2/1 locked magnetic islands is easily produced by the increasing of viscous item (ω_0) and decreasing of electromagnetic item (coupling).

Acknowledgements

This work was supported by National MCF Energy R&D Program under Contract (Nos. 2019YFE03020000, 2018YFE0304100), National Nature Science Foundation of China under Grant (Nos. 12175271, 11975267, 11975273).

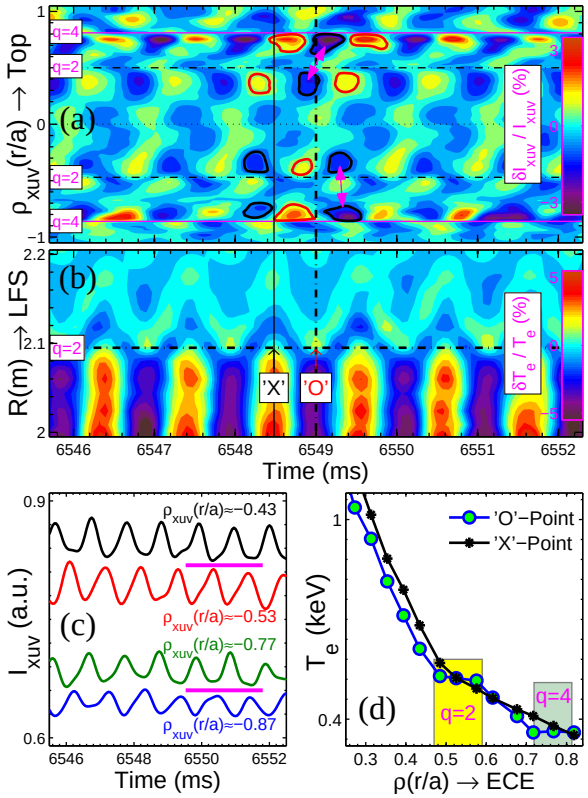

FIG. 13: The $m/n = 2/1$ and $m/n = 4/1$ magnetic islands are coupled together and rotated by the same frequency. (a) and (b) are the fluctuations of $\delta I_{xuv}/\bar{I}_{xuv}$ and $\delta T_e/\bar{T}_e$, (c) is the raw XUV signals, and the T_e-profiles of 'O' and 'X' points of magnetic islands for similar discharge condition are given in (d).

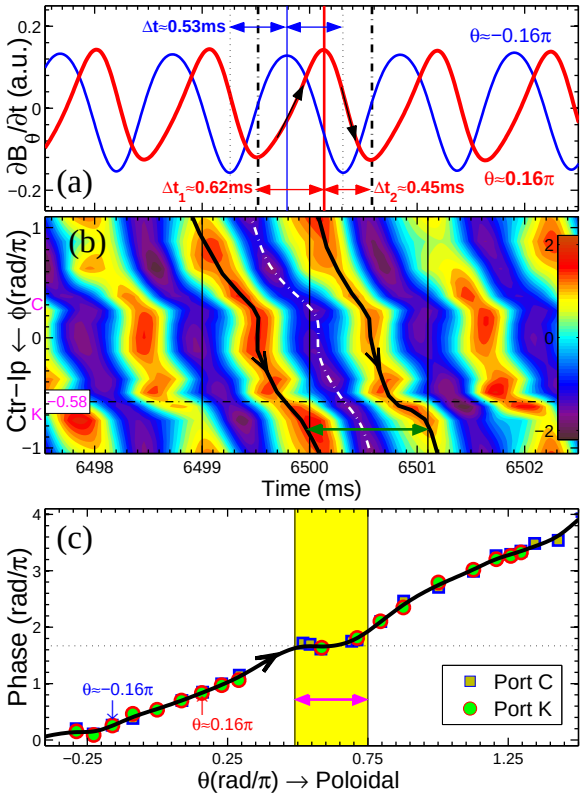

FIG. 14: The asymmetric structure is caused by the interaction with tungsten protector limiter. Note: the 3D asymmetric index $\gamma_{3Da} \equiv \Delta t_1/\Delta t_2$ is defined, and the $\gamma_{3Da} \approx 1$ and $\gamma_{3Da} \approx 1.4$ for the two poloidal positions of $\theta = -0.16\pi$ and $\theta = 0.16\pi$ respectively.

Appendix

A. Modes coupling

The electromagnetic coupling of multiple helicities of magnetic islands at different rational surfaces are observed. The $m/n = 4/1$ magnetic islands can be excited once again during the outward transport of low-Z impurity concentration, which is fully coupled to the $m/n = 2/1$ magnetic islands after the unlocked of $m/n = 2/1$ LMs, as shown in figure 13. The radial position of magnetic islands can be featured by the minimum fluctuations of $\delta I_{xuv}/I_{xuv}$ and $\delta T_e/T_e$, e.g., the $\delta I_{xuv}/I_{xuv} \approx 0$ and $\delta T_e/T_e \approx 0$ are observed for the same region of q = 2 surface. The $\delta I_{xuv}/I_{xuv} \approx 0$ can also be observed for the region $\rho_{xuv}(r/a) \approx \pm 0.8$ of q = 4 surface, and the phase difference is reversed on both sides of q = 2, 4 surfaces are demonstrated in figure 13(c). The modes coupling of different helicities of magnetic islands at q = 2, 4 surfaces is also observed by the ECE array for the similar discharge condition as shown in figure 13(d), which is confirmed by the measurement of Doppler backscattering (DBS) array as Ref [33]. The coupling of $m/n = 2/1$ and $m/n = 4/1$ magnetic islands are rotated by the same frequency $f_{2/1}$ as demonstrated in figure 14. Therefore, the application of the formula $w \propto \delta B_\theta^{1/2}$ [34, 35] should be cautious in current condition (#61042), e.g., the magnetic oscillation amplitude are $\delta B_\theta \approx 1.7$ Gauss and $\delta B_\theta \approx 3.7$ Gauss respectively for the two moments of t ≈ 3.64 s and t ≈ 6.5 s, while the width of $m/n = 2/1$ magnetic islands for the two cases are nearly the same as $w \approx 5$ cm.

The phase displacement of $m/n = 2/1$ and $m/n = 4/1$ magnetic islands are deviated from each other. The 'O'-points of those magnetic magnetic islands at the q = 2, 4 surfaces are mismatched and in-phase along the poloidal (vertical) and radial (horizontal) directions respectively, as demonstrated in figure 13 (a) and (d). The primary reason should be caused by the different helicities of $m/n = 2/1$ and $m/n = 4/1$ magnetic islands, and the snake-like fluctuation with $\delta T_e/T_e \approx 1\%$ can be observed in the annular region $0.5 \le \rho \le 0.8$ as shown in figure 13(b). The brake torque F_{RW} between the tungsten protector limiter and the $m/n = 2/1$ magnetic islands should be weakened by the electromagnetic coupling of of those magnetic islands. Furthermore, the poloidal symmetry of $m/n = 2/1$ magnetic islands is also broken, e.g., the 'X' and 'O' points of magnetic islands are observed simultaneously for the bottom and top sections respectively.

B. 3D asymmetry (3Da)

The 3D asymmetric structure of the coupled of $m/n = 2/1$ and $m/ = 4/1$ magnetic islands is observed. The coupled magnetic islands are propagated in the counter-current (toroidal) and counter-clockwise (poloidal) directions re-

spectively, and the mode numbers are $n = 1$ and $m = 2$. The oscillation of magnetic signals are caused by the rotation of magnetic islands, and the structure of sinusoidal signal is observed for the bottom section with $\theta \approx -0.16\pi$, as shown in figure 14(a). However, the symmetric structure is broken on the top section, and the magnetic signal ascends slowly and descends swiftly that is featured by $\Delta t_1 > \Delta t_2$. The 3D asymmetric index is defined as: $\gamma_{3Da} \equiv \Delta t_1/\Delta t_2$, and the index are $\gamma_{3Da} \approx 1$ and $\gamma_{3Da} \approx 1.4$ respectively for the for the two poloidal positions of $\theta = -0.16\pi$ and $\theta = 0.16\pi$. The rotation velocity ($v = d\phi/dt$) of those magnetic islands is nonuniform along toroidal direction, which increases swiftly and decreases obviously for the two inflection points of $\phi \approx 0.3\pi$ and $\phi \approx -0.58\pi$ respectively. Similarity, such structure is reproduced by the poloidal magnetic pickup array, and the two special regions of $-0.58\pi \leq \phi \leq 0.3\pi$ and $0.5\pi \leq \theta \leq 0.75\pi$ are observed for the toroidal and poloidal directions respectively. The primary reason should be caused by the interaction with the tungsten protector limiter, namely the rotation velocity of those magnetic islands is accelerated and decelerated respectively when approach to and deviate from the tungsten protector limiter.

[1] J. S. Hu *et al.*, Physical Review Letters **114**, 055001 (2015).
[2] W. L. Zhong *et al.*, Physical Review Letters **117**, 045001 (2016).
[3] G. Z. Zuo *et al.*, Nuclear Fusion **59**, 016009 (2019).
[4] A. Kallenbach *et al.*, Plasma Physics and Controlled Fusion **55**, 124041 (2013).
[5] W. Suttrop *et al.*, Nuclear Fusion **37**, 119 (1997).
[6] D. A. Gates and L. Delgado-Aparicio, Physical Review Letters **108**, 165004 (2012).
[7] D. A. Gates, L. Delgado-Aparicio, and R. B. White, Nuclear Fusion **53**, 063008 (2013).
[8] L. Xu *et al.*, Nuclear Fusion **57**, 126002 (2017).
[9] M. Xu *et al.*, Nuclear Fusion **58**, 124004 (2018).
[10] H.-W. Xu *et al.*, Plasma Physics and Controlled Fusion **62**, 105009 (2020).
[11] M. A. Van Zeeland *et al.*, Nuclear Fusion **48**, 092002 (2008).
[12] M. Nave and J. Wesson, Nuclear Fusion **30**, 2575 (1990).
[13] R. B. White, D. A. Gates, and D. P. Brennan, Physics of Plasmas **22**, 022514 (2015).
[14] Y. Huang *et al.*, Nuclear Fusion **58**, 126024 (2018).
[15] F. L. Waelbroeck and R. Fitzpatrick, Physical Review Letters **78**, 1703 (1997).
[16] R. Fitzpatrick, Physics of Plasmas **22**, 092506 (2015).
[17] H. Jin *et al.*, Plasma Physics and Controlled Fusion **57**, 104007 (2015).
[18] V. Klevarov *et al.*, Plasma Physics and Controlled Fusion **62**, 025024 (2019).
[19] R. J. L. Haye *et al.*, Nuclear Fusion **46**, 451 (2006).
[20] H. Zohm, *Magnetohydrodynamic Stability of Tokamaks* (Viley-VCH, Germany, 2014).
[21] V. Igochine, *Active Control of Magneto-hydrodynamic Instabilities in Hot Plasmas* (Springer, Berlin, 2015), Vol. 83.
[22] Z. Xu *et al.*, Review of Scientific Instruments **87**, 11D429 (2016).
[23] L. Zhang *et al.*, Review of Scientific Instruments **86**, 123509 (2015).
[24] Y. M. Duan *et al.*, Review of Scientific Instruments **83**, 093501 (2012).
[25] H. Q. Liu *et al.*, Review of Scientific Instruments **87**, 11D903 (2016).
[26] X. Han *et al.*, Review of Scientific Instruments **85**, 073506 (2014).
[27] Y. Liu *et al.*, Fusion Engineering and Design **136**, 72 (2018).
[28] Q. Zang *et al.*, Nuclear Fusion **56**, 106003 (2016).
[29] B. N. Wan *et al.*, Nuclear Fusion **57**, 102019 (2017).
[30] H.-H. Wang *et al.*, Nuclear Fusion **56**, 066011 (2016).
[31] R. C. Isler, Nuclear Fusion **24**, 1599 (1984).
[32] J. E. Rice *et al.*, Nuclear Fusion **58**, 126008 (2018).
[33] M. Xu *et al.*, Nuclear Fusion **61**, 036034 (2021).
[34] T. Shi *et al.*, Plasma Physics and Controlled Fusion **55**, 055007 (2013).
[35] F. Salzedas, F. C. Schller, A. A. M. Oomens, and R. T. P. T. the, Physical Review Letters **88**, 075002 (2002).